ORNL/TM-2021/2026

Performance of Embedded Sensors in 3D Printed SiC

Christian M. Petrie
Adrian M. Schrell
M. Dylan Richardson
Holden Hyer
Gokul Vasudevamurthy

June 2021

M3TC-21OR0404042

OAK RIDGE National Laboratory

ORNL IS MANAGED BY UT-BATTELLE LLC FOR THE US DEPARTMENT OF ENERGY

ORNL/TM-2021/2026

Transformational Challenge Reactor Program

PERFORMANCE OF EMBEDDED SENSORS IN 3D PRINTED SIC

Christian M. Petrie
Adrian M. Schrell
M. Dylan Richardson
Holden Hyer
Gokul Vasudevamurthy

June 2021

M3TC-21OR0404042

Prepared by
OAK RIDGE NATIONAL LABORATORY
Oak Ridge, TN 37831-6283
managed by
UT-BATTELLE LLC
for the
US DEPARTMENT OF ENERGY
under contract DE-AC05-00OR22725

CONTENTS

ACKNOWLEDGMENTS

This research was sponsored by the Transformational Challenge Reactor (TCR) program of the US Department of Energy (DOE) Office of Nuclear Energy. The report was authored by UT-Battelle under Contract No. DE-AC05-00OR22725 with DOE. Michael Trammell assisted with binder jet printing of the SiC components. Austin Schumacher and Brian Jolly supported some of the early chemical vapor infiltration work. Ying Yang performed computational thermodynamic calculations during the initial material selection stages. Donovan Leonard performed experimental characterizations of the early material compatibility specimens, and Andrés Márquez Rossy performed scanning electron microscopy of an embedded functional sensor. Michael Russell and Mark Vance assisted with the quality assurance procedures and the test plan. Kurt Terrani contributed to the initial concept for embedding sensors and provided technical direction throughout the technology development process.

ABSTRACT

This report summarizes recent advances in embedding sensors in 3D printed silicon carbide (SiC) ceramic components under the Transformational Challenge Reactor (TCR) program. The additive manufacturing technologies developed under this program will enable fabrication of complex structures with embedded fuels and sensors. The sensors will be capable of characterizing fuel performance using spatially distributed measurements at the most strategic locations that would be otherwise inaccessible using conventional manufacturing techniques. While previous programmatic updates describe initial concepts for embedding sensors, materials selection, and initial characterization of the embedded sensors, the technology requires further demonstration, and quality-significant procedures must be established before the embedding technology is ready for adoption by industry. To this end, this report describes the most effective techniques that have been used to embed functional sensors in 3D printed components using a combination of binder-jet additive manufacturing and chemical vapor infiltration (CVI). A detailed procedure describes each step in the process and is available upon request. Molybdenum (Mo)-sheathed thermocouples have been successfully embedded in complex SiC components, and temperatures were monitored in situ during the embedding process. Post-embedding measurements showed no significant hysteresis, and characterization of the interface revealed qualitatively strong bonding around the entire perimeter of the sensor sheath. Distributed fiber-optic temperature sensors were able to briefly measure temperature profiles during CVI, but they ultimately failed prior to completion of the CVI run. The failure appears to be related to the fiber coating at temperatures close to 1,000°C. Future work will focus on irradiation testing of embedded thermocouples and other sheathed electrical sensors, as well as the identification of fiber-optic sensor coatings that can survive CVI.

1. INTRODUCTION

Conventional nuclear reactors and power plants generally require a limited number of sensors to monitor and control reactor power. These include basic monitoring of inlet and outlet coolant temperatures, coolant flow rates, core internal pressure, and neutron flux. Recent interest in microreactors—which are physically smaller and operate at greatly reduced thermal power levels—has been driven by the desire to reduce both capital and operation and maintenance costs to increase the economic competitiveness of nuclear power plants [1]. The smaller size of microreactors will naturally reduce the volume available for locating in-core sensors. Perhaps more importantly, microreactors would ideally be more highly instrumented to provide more information to operators and reduce the number of onsite staff required to operate, inspect, and maintain the plant. One emerging technology that could provide more significant benefits to microreactors is embedding sensors directly within metal or ceramic components to directly probe components or structures. Embedded sensors could be used for health monitoring of components or systems to provide real-time data during operation, potentially leveraging sensing technologies that provide spatially distributed measurements. Such monitoring capabilities could greatly improve upon the scarce, single-point measurements currently available, ultimately leading to more informed operational decision-making capabilities through enhanced diagnostics and prognostics.

Additive manufacturing (or 3-D printing) technologies are particularly attractive for embedding sensors within components at locations that would be inaccessible using conventional manufacturing techniques [2-5]. For example, in a traditional light water reactor, the centerline of the UO_2 fuel pellets is the highest temperature location in the core. Because fuel centerline temperatures can dictate some reactor operating limits, the ability to directly monitor peak fuel temperatures would be extremely useful for operational decision making. Because of the challenges associated with drilling holes in brittle, uranium-bearing ceramics and passing sensor leads through the pressure boundary of the zirconium alloy fuel cladding, measurements of fuel centerline temperatures are not typically made during reactor operation. Therefore, peak fuel temperatures can only be estimated based on thermomechanical models and limited irradiation testing that is performed in test reactors during the fuel qualification process [6]. This limitation leads to overly conservative limits on fuel loading and operational flexibility based on conservative calculations of core power distributions and fuel performance. Figure 1 illustrates the concept with contours indicating qualitative variations in fuel temperatures and neutron flux (due to self-shielding effects) [4]. The ability to embed sensors within fueled structures to directly monitor local temperatures and reactor power could greatly reduce these conservatisms and expand the possibilities for designing new reactors and refueling existing reactors. Additive manufacturing technologies could also be used to fabricate sensors with features that cannot easily be incorporated using traditional manufacturing approaches [7-9].

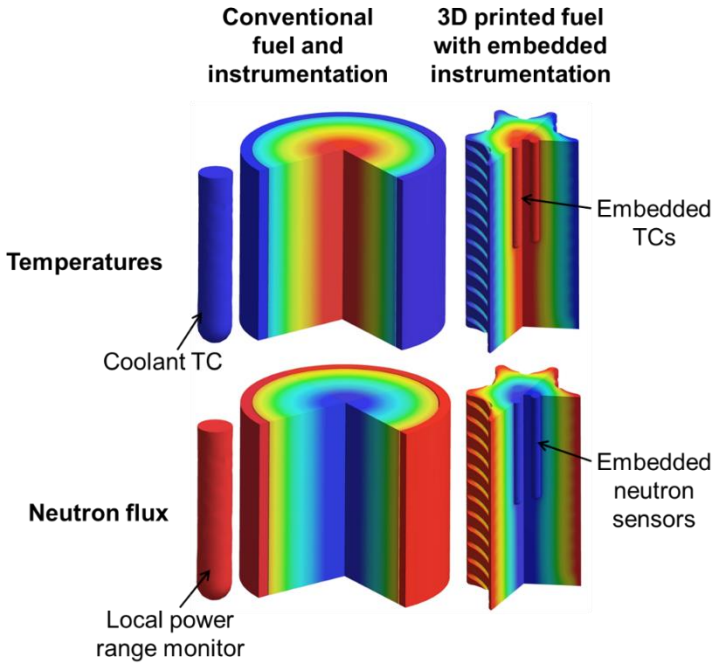

Figure 1. Conceptual schematic showing qualitative maps of temperature and neutron flux and the location of instrumentation in conventional fuel vs. 3D-printed fuel with embedded instrumentation. Reprinted with minor modifications from *Journal of Nuclear Materials*, Vol 552, C.M. Petrie, A.M. Schrell, D.N. Leonard, Y. Yang, B.C. Jolly, and K.A. Terrani, "Embedded sensors in additively manufactured silicon carbide," Page 153012, Copyright (2021), with permission from Elsevier [4]**.**

Oak Ridge National Laboratory's (ORNL's) Transformational Challenge Reactor (TCR) is being designed to leverage a novel 3D-printing process that was developed to fabricate complex silicon carbide (SiC) ceramic structures with embedded fuel particles [10-12]. The fabrication process also allows for direct embedding of sensors, in addition to fuel [4]. SiC has long been considered for a wide range of nuclear applications due to its high-temperature strength [13], resistance to oxidation in steam and water [14, 15], mechanical and dimensional stability under neutron irradiation [16-19], and low parasitic neutron absorption [20]. However, its use has been limited in part due to challenges in manufacturing geometries other than simple plates, tubes, or rods. The 3D printing process developed under the TCR Program has enabled the manufacturing of complex SiC structures [21] and now offers the ability to directly embed both fuels and sensors during the manufacturing process. However, these technologies are only useful if they are technologically ready for adoption by the nuclear industry. Therefore, recent programmatic efforts have been focused on moving these technologies beyond the initial concept and feasibility stage and advancing their technological readiness to the point where quality significant procedures are established and can be handed off to industrial partners. To this end, this report summarizes the performance of embedded sensors in additively manufactured silicon carbide (SiC) ceramic components and the procedures that have been developed to enable commercial deployment of this technology. A separate document, available upon request, provides a detailed description of the sensor embedding procedure.

2. METHODS

2.1 SENSOR-EMBEDDING PROCESS

The sensor embedding process has been discussed in detail in a published paper [4] and is addressed in several previous reports [22, 23]. Briefly, complex SiC geometries are created using a binder jet additive manufacturing process that builds the part from a sliced 3D computer aided design (CAD) model. After a bed of SiC powder has been raked, a liquid binding agent is deposited over the solid portions of each slice and then the bed is lowered before the process moves to the next slice. After the printing process is complete, the bed is heated to ~190°C to cure the binder, the part is then excavated from the powder bed, and any excess powder is removed. Although several approaches were considered early in the program [23], two approaches have shown the most promise. In the first approach, the part is printed with a true-sized cavity, and the sensor is pressed into the cavity after binder jet printing. Examples of this are shown in Figure 2a and Figure 2b. In the second approach, an oversized cavity is printed, the sensor is inserted into the cavity, and the remaining cavity volume is filled with loose SiC powder. This second approach is shown in Figure 2c and Figure 2d.

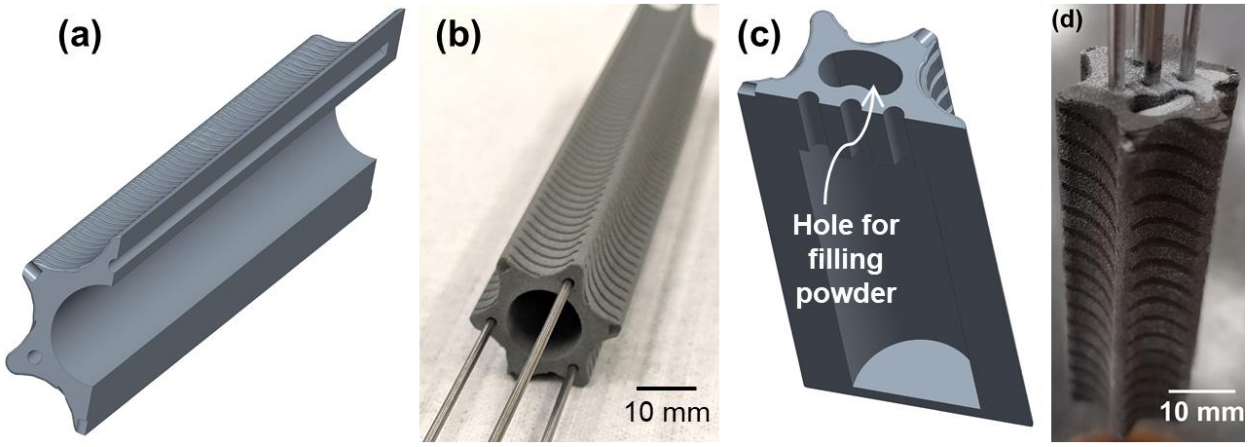

Figure 2. Sectioned CAD views (a,c) and pictures (b,d) showing the component printing and sensor embedding process when printing a true-sized cavity (a,b) or an oversized cavity with the free volume filled with loose SiC powder (c,d). Reprinted with minor modifications from *Journal of Nuclear Materials*, Vol 552, C.M. Petrie, A.M. Schrell, D.N. Leonard, Y. Yang, B.C. Jolly, and K.A. Terrani, "Embedded sensors in additively manufactured silicon carbide," Page 153012, Copyright (2021), with permission from Elsevier [4].

After using either approach to install the sensor in the printed part, the entire assembly is densified using chemical vapor infiltration (CVI). This process flows methytrichlorisane (MTS) gas carried by hydrogen (H_2) into a reactant chamber, where the MTS thermally decomposes to form crystalline SiC plus hydrochloric acid (HCl). In addition to densifying the part by depositing crystalline SiC in the pores between the powder granules, the infiltration process also bonds the sensor to the surrounding SiC matrix. For relatively thin parts (<1 cm), SiC matrix densities greater than 90% of the theoretical value can be achieved [21]. A detailed procedure for embedding sensors is available in a separate document that is available upon request.

This report focuses on embedding of molybdenum (Mo)-sheathed thermocouples and fused silica optical fiber-based temperature sensors. Previous works describe efforts to directly embed fiber-optic strain sensors and niobium (Nb)-sheathed thermocouples [5, 22]. The successful embedding of Mo-sheathed thermocouples, described later in this report, eliminates the need to pursue embedding of Nb-sheathed thermocouples. Nb-sheathed thermocouples are not as readily available and can suffer from embrittlement due to grain growth during high temperature heat treatments or due to hydride formation in the low

temperature region of the CVI system [4]. Fiber-optic strain sensors are still of interest, but additional work is required to properly embed the fibers directly in a SiC matrix. As described below, future efforts will first focus on embedding sheathed fiber-optic sensors before addressing direct embedding of fiber-optic strain sensors.

2.2 IN SITU DATA COLLECTION

As described in previous works [22, 23], a custom flange was designed for the CVI system to allow instrument penetrations for in situ monitoring during the sensor embedding and SiC densification process. The CVI process involves an initial ramp to the temperature set point in an argon environment, followed by introduction of MTS and H_2. The process typically operates at nominal temperatures of 1,000°C, and this usually lasts for several days to ensure that the parts are properly infiltrated.

Both Type C thermocouples and fused silica-based distributed fiber-optic temperature sensors in molybdenum sheaths were interrogated during the CVI process. Thermocouples were logged every 10 seconds during testing using a commercially available data acquisition system. The fiber-optic sensors relied on Rayleigh backscattering from ordinary SMF-28 singlemode fiber interrogated using an Optical Backscatter Reflectometer (OBR, model 4600 from Luna Innovations Inc.) [24, 25]. The OBR data were logged approximately once per minute and processed using a recently demonstrated adaptive reference technique that enables reconstruction of distributed temperatures up to 950°C or higher [26]. The spectral shifts measured using the OBR were converted to changes in temperature using a calibration that was developed for the same type of fiber using a Type K thermocouple.

2.3 POST-EMBEDDING CHARACTERIZATION

In addition to taking pictures of the samples with embedded sensors after the CVI process, one sample was sectioned and polished for additional characterization. Sections were taken along the sensor's axis and in a transverse plane to evaluate the interface between the Mo sheath and the SiC matrix. Characterization included imaging with a scanning electron microscope and energy dispersive x-ray spectroscopy (EDS) to look for evidence of chemical interactions between the sheath and the matrix. Previous characterizations of embedded tubes and coupons showed a thin (<10 μm) molybdenum silicide layer that formed at the outer surface of the sheath [4]. Additional characterization was performed on embedded functional sensors to ensure that the silicide layer did not increase in thickness, which could embrittle the sensor sheath. Finally, microindentation was performed on the embedded thermocouple sheath and nanoindentation was performed across the SiC-Mo interface to provide more insight into the interfacial strength.

3. RESULTS

3.1 EMBEDDING OF FUNCTIONAL THERMOCOUPLES

Figure 3 shows pictures of a Type C Mo-sheathed thermocouple after embedding. Two thermocouples were successfully embedded by printing a true-sized hole using binder jet and pressing the thermocouple into the hole prior to CVI—similar to what is shown in Figure 2a and Figure 2b. As discussed further in Section 3.2, the embedded thermocouples remained functional throughout the CVI process and showed no signs of hysteresis. The bonding from the thermocouple to the SiC matrix qualitatively appears to be quite strong, as the thermocouple cannot be separated from the matrix by hand. In fact, one of the thermocouples remained bonded to its surrounding matrix even after the SiC part fractured below the embedded thermocouple during disassembly (see Figure 4). This implies that the bond strength actually exceeds the fracture strength of the printed SiC material. This type of fracture has also been seen in other infiltrated SiC parts when the parts bond to the underlying support during CVI. It is suspected that this bonding was more significant for the part that fractured, because thermal expansion of the sensor sheath—which was constrained in the flange at the top of the CVI system—put additional pressure on the interface between the part and the underlying support. Additional work is being performed to more quantitatively characterize the strength of the SiC to Mo bonding (see Section 3.3). The only other visible effect on the sensor is a thin, shiny layer of SiC that was deposited along a portion of the sensor sheath.

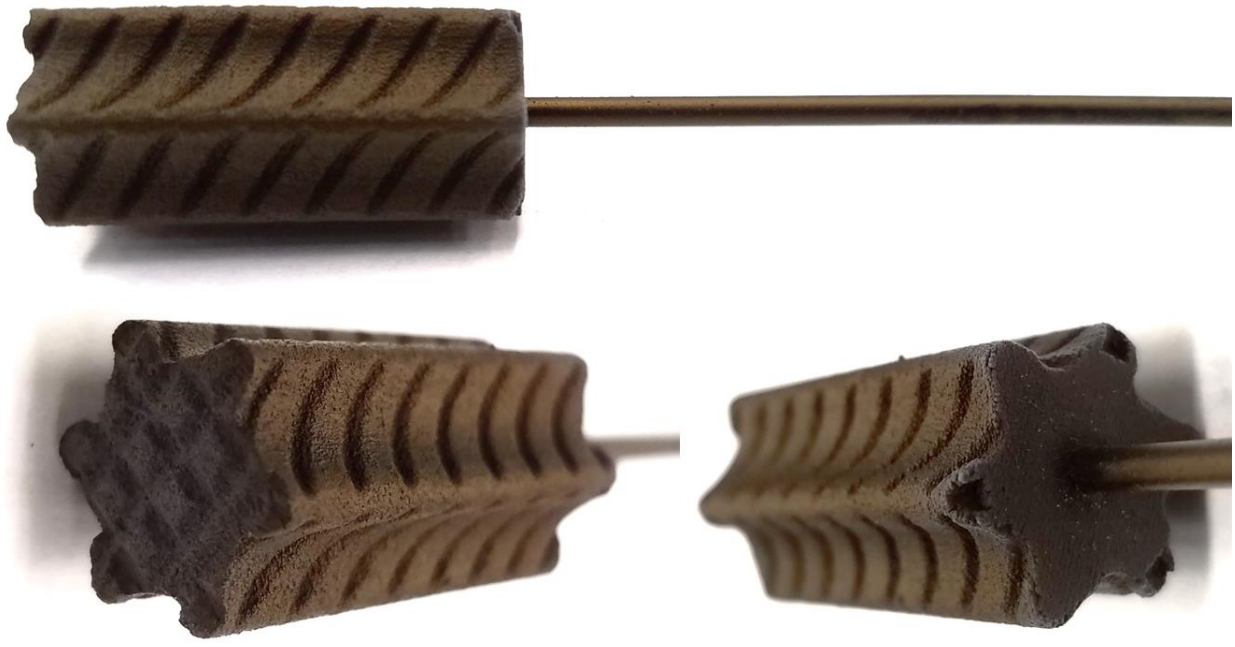

Figure 3. Pictures of embedded functional thermocouples. Reprinted with minor modifications from *Journal of Nuclear Materials*, Vol 552, C.M. Petrie, A.M. Schrell, D.N. Leonard, Y. Yang, B.C. Jolly, and K.A. Terrani, "Embedded Sensors in Additively Manufactured Silicon Carbide," Page 153012, Copyright (2021), with permission from Elsevier [4].

Figure 4. Picture of a successfully embedded thermocouple in a SiC part that fractured during disassembly due to the part bonding to the underlying support.

3.2 IN SITU MEASUREMENTS DURING INFILTRATION

Figure 5 shows in situ measurements of temperatures recorded using an embedded thermocouple during a five day CVI run. Results are shown for the entire experiment and during the period of operation close to the 1,000°C set point, which is shown as a dashed black line. The furnace was controlled using thermocouples located external to the quartz tube in which the parts are located and the reactant gases flow. The embedded thermocouple approached the set point temperature until around 6.3 hours, which is when the process gas was switched from argon to a mixture of MTS and H_2. The embedded sensor showed that the temperature decreased slightly, most likely due to the lower density and higher thermal conductivity of hydrogen, which increased axial heat losses and potentially natural convection flow inside the quartz tube. Further evidence supporting this theory is shown near 98 hours, when there was a temporary loss of MTS and H_2 flow. This caused the temperatures to increase briefly until slightly after 99 hours, when the flow of MTS and H_2 was restored, and the temperatures decreased once again. After the CVI run was complete and the furnace cooled to near room temperature, the embedded thermocouple read within 1°C of the external thermocouples, indicating that no significant hysteresis occurred in the embedded thermocouple as a result of embedding.

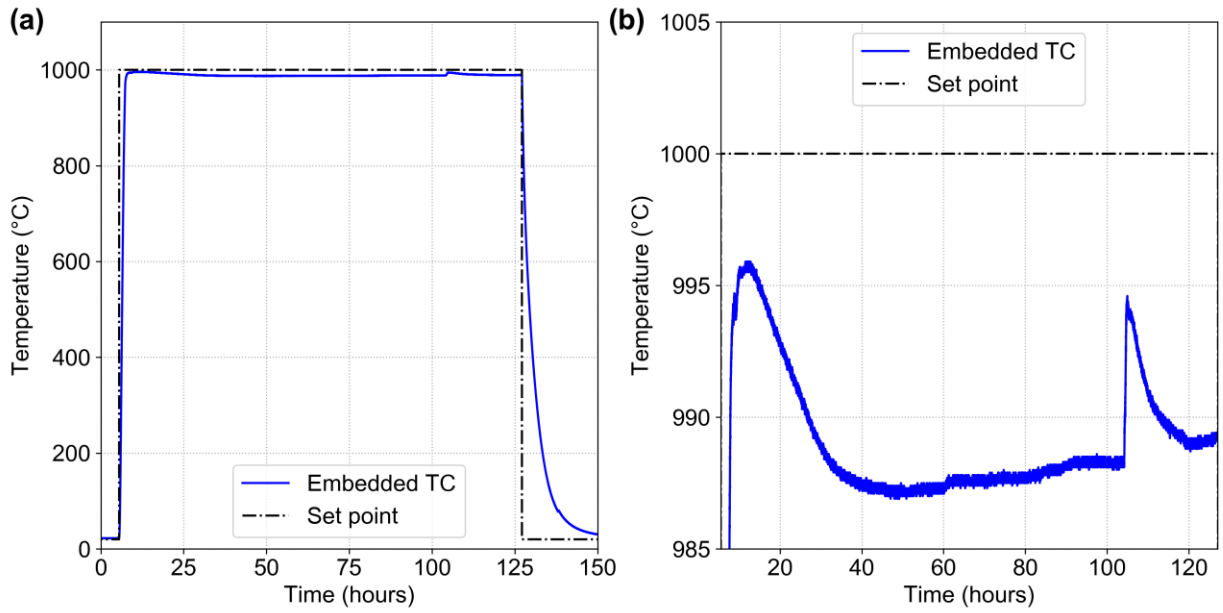

Figure 5. Temperatures measured in situ during CVI by the first Mo-sheathed embedded thermocouple (TC). Reprinted with minor modifications from *Journal of Nuclear Materials*, Vol 552, C.M. Petrie, A.M. Schrell, D.N. Leonard, Y. Yang, B.C. Jolly, and K.A. Terrani, "Embedded sensors in additively manufactured silicon carbide," Page 153012, Copyright (2021), with permission from Elsevier [4].

Figure 6 shows the temperatures measured in situ during embedding of a second Mo-sheathed thermocouple over a four-day CVI run. In a manner similar to that observed previously (**Figure 5**), the temperature of the embedded thermocouple approached the 1,000°C set point and then decreased once MTS and H_2 flow was introduced. There was a brief interruption in the logging of the thermocouple data between 52 and 72 hours, but it was clear that the temperatures eventually approached a steady-state value of ~981°C. Like the first embedded thermocouple, this sensor survived CVI with no evidence of hysteresis. Based on the successful embedding of thermocouples and the lack of hysteresis observed after CVI, the embedding of electrically based sensors such as thermocouples or self-powered neutron detectors with Mo sheaths is now considered mature enough to warrant neutron irradiation testing. Such testing will be considered in future work.

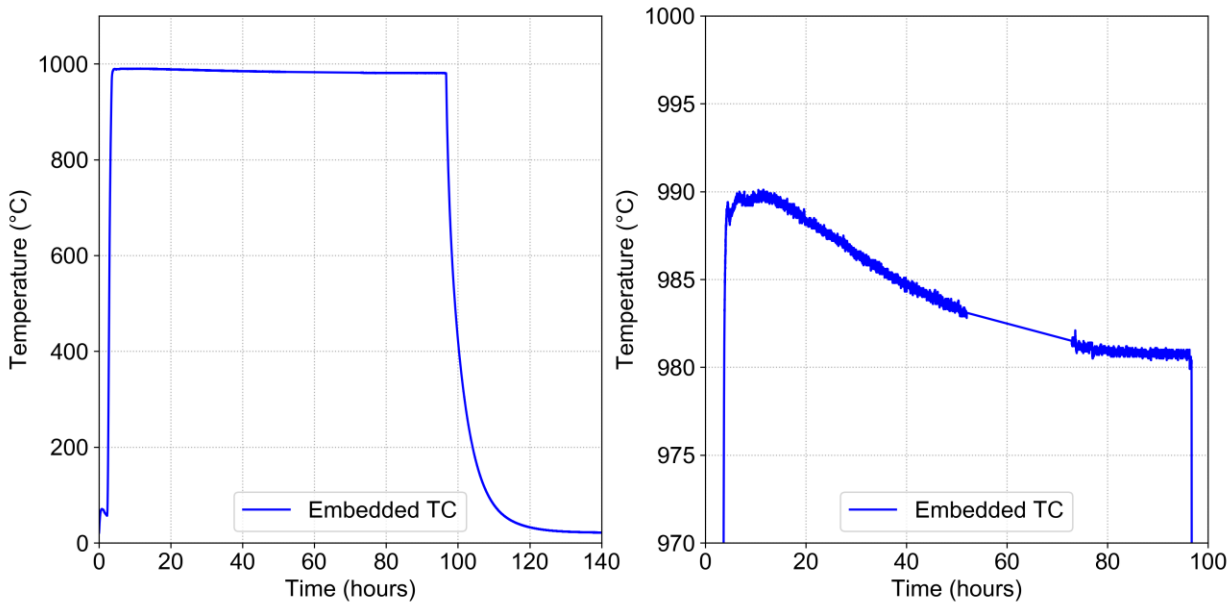

Figure 6. Temperatures measured in situ during CVI by the second Mo-sheathed embedded thermocouple (TC).

Because previous tests of embedded fiber-optic temperature sensors showed mechanical failure of the fibers during the first day of CVI, an additional test was performed using a fiber-optic sensor located in the CVI run but not embedded in a SiC part. This was done to separate issues related to constrained expansion of the sensor sheath vs. issues related only to operation of the fiber inside a Mo sheath at the process temperatures. Figure 7 shows spatial temperature profiles relative to the center of the furnace as a function of time during a portion of the first day of a CVI run. Flow transitioned from argon to H_2 + MTS near 269 minutes, resulting in a reduction in temperatures similar to that observed in Figure 5 and Figure 6. However, the fiber-optic sensors were able to measure the temperature profile over a much larger spatial region. Figure 8 shows two-dimensional plots of the temperature profile at various times during CVI. Temperatures are shown as measured by the fiber-optic sensors, as well as a thermocouple that was placed closer to the vertical midplane of the furnace. The increases in the temperatures further from the vertical midplane of the furnace are consistent with the idea that introducing H_2 into the furnace increases axial heat losses, which would increase temperatures outside of the actively heated region.

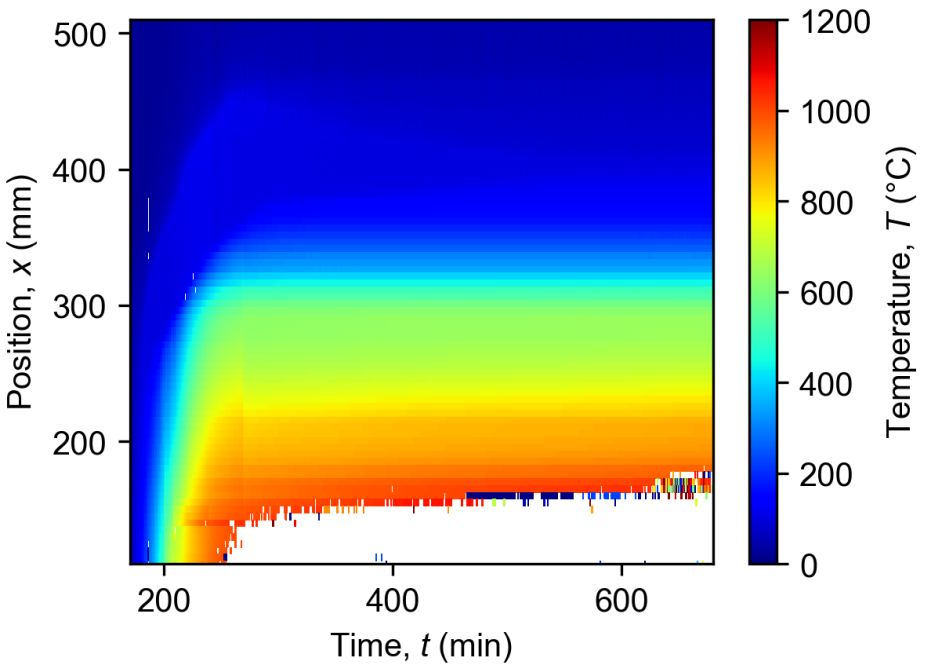

Figure 7. Spatially distributed temperatures measured during a portion of the first day of a CVI run using fiber-optic sensors. Positions are relative to the vertical midplane of the furnace and H_2 + MTS flow was initiated near 269 minutes. White regions of the plot correspond to locations for which the sensors could not resolve a temperature change due to a lack of correlation between the fiber-optic signal and an earlier reference scan.

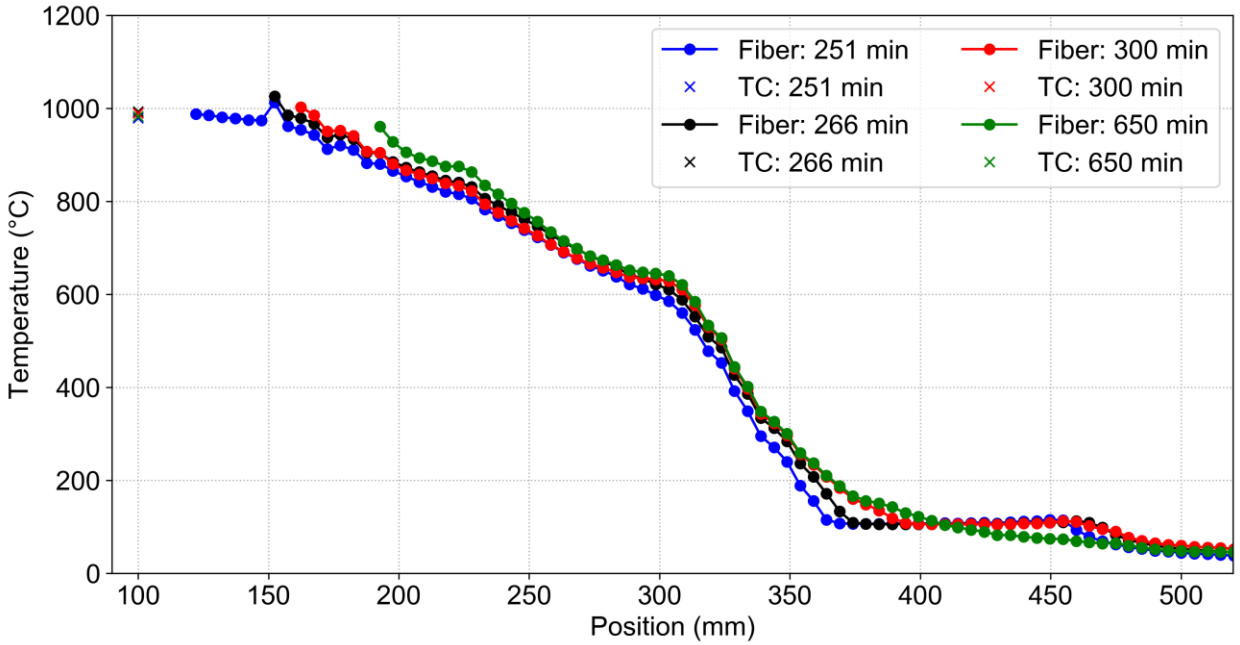

Figure 8. Temperature profiles measured using fiber-optic sensors and a thermocouple (TC) during the first day of a CVI run at various times.

The white regions of Figure 7 correspond to locations where the reflected fiber-optic signal could not be well correlated to previous reference scans, resulting in an ability to accurately resolve the temperature. These missing data are also reflected in Figure 8. The white regions gradually increased in size as more of

the fiber could not be resolved. To illustrate why a larger portion of the fiber could not be resolved with increasing time during CVI, Figure 9 shows contour plots of the reflected signal amplitude vs. time and position. These data show that the amplitude increased significantly in the high temperature region, particularly at positions closest to the furnace's vertical midplane (i.e., smallest values of x). Eventually the fiber broke at these same locations. Therefore, it is suspected that the fiber was becoming increasingly strained at these locations, which resulted in increased light reflections, until eventually the fiber broke. Increased light reflections would interfere with the Rayleigh backscattered light that is analyzed to perform the distributed temperature measurements and prevent the post-processing algorithm from being able to correlate spectral changes due to thermal expansion and changes in the fiber's refractive index. The reason for the increased strain and eventual breaking of the fiber is suspected to be related to the polymer-based coatings, although it is possible that the silica glass is directly interacting with the Mo sheath where the fiber contacts the sheath. To confirm this, future experiments will test fibers with metal coatings and bare (uncoated) fibers.

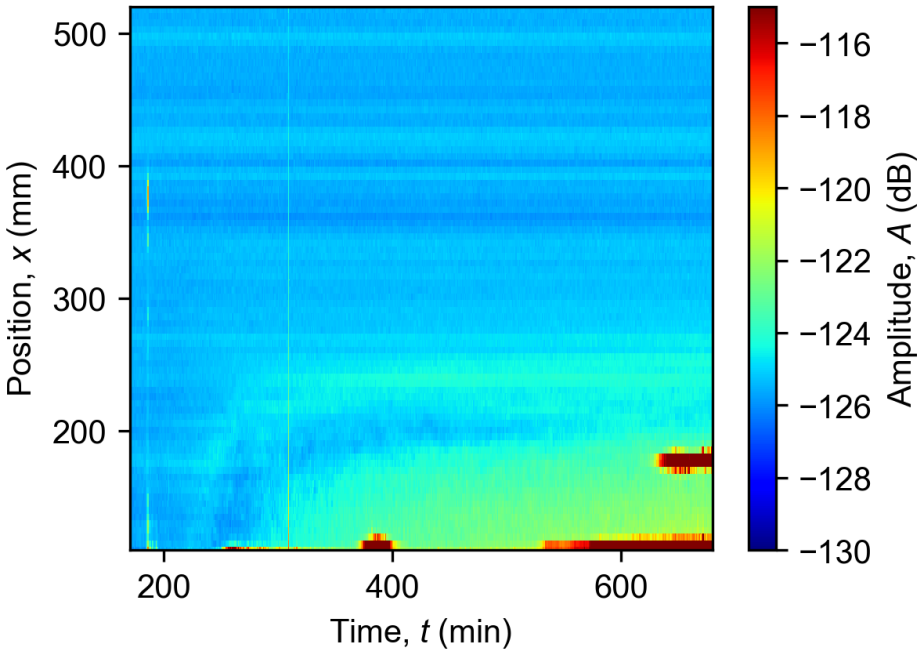

Figure 9. Reflected fiber-optic signal amplitude vs. time and position relative to the vertical midplane of the furnace during a portion of the first day of CVI.

3.3 POST-EMBEDDING CHARACTERIZATION

Because the 3D printed SiC component containing the second embedded thermocouple broke during disassembly, this part was sectioned through the embedded region of the thermocouple so that it could be further characterized. Figure 10 shows scanning electron microscope images of sections taken along and perpendicular to the sensor's axis. Near the Mo-SiC interface, the microstructure and porosity of the SiC matrix is very similar to that of the bulk microstructure further away from the interface, indicating that the part was well infiltrated near the sensor interface. The interface also generally appears similar around the entire perimeter of the sensor's outer surface, although there is slightly higher porosity near the interface in the lower right portion of Figure 10a. These images are consistent with previous qualitative observations of strong bonding between the sensor and the SiC matrix.

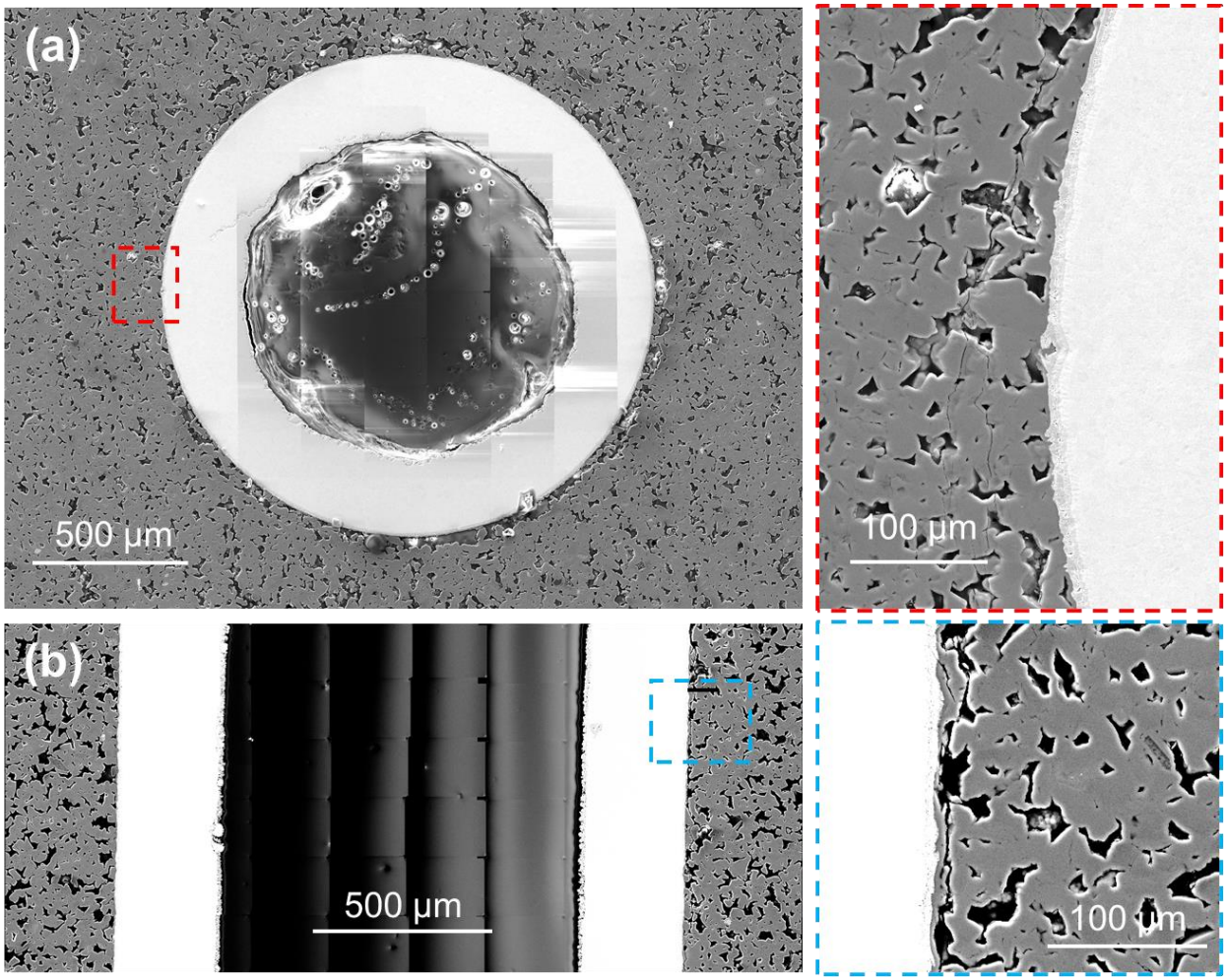

Figure 10. Scanning electron microscope images of a 3D printed SiC part with an embedded Mo sheathed thermocouple sectioned perpendicular (a) and parallel (b) to the sensor's axis.

The sectioned parts with an embedded thermocouple were further characterized to ensure that there were no obvious signs of chemical interaction between the Mo sensor sheath and the SiC matrix. Figure 11 shows EDS elemental maps near a portion of the Mo–SiC interface. Unfortunately, there is not much contrast in the carbon maps because of the high carbon content in the epoxy that filled the porous regions during the specimen preparation. In fact, the carbon content in the SiC on the left side of the images is indistinguishable from the carbon content in the Mo on the right side of the image. The Mo and Si maps clearly show some chemical interaction, as the Si content increases moving from right to left from the Mo sheath to the SiC matrix. Similarly, the Mo content decreases moving in the same direction. Fortunately, the thickness of the interaction layer is limited to ~10 µm, which is consistent with previous results [4]. For an approximately 270 µm thick sheath, this thickness would not have a significant effect on the mechanical properties of the sensor. It is likely that this chemical interaction plays a role in the strength of the bonding between the sheath and the matrix.

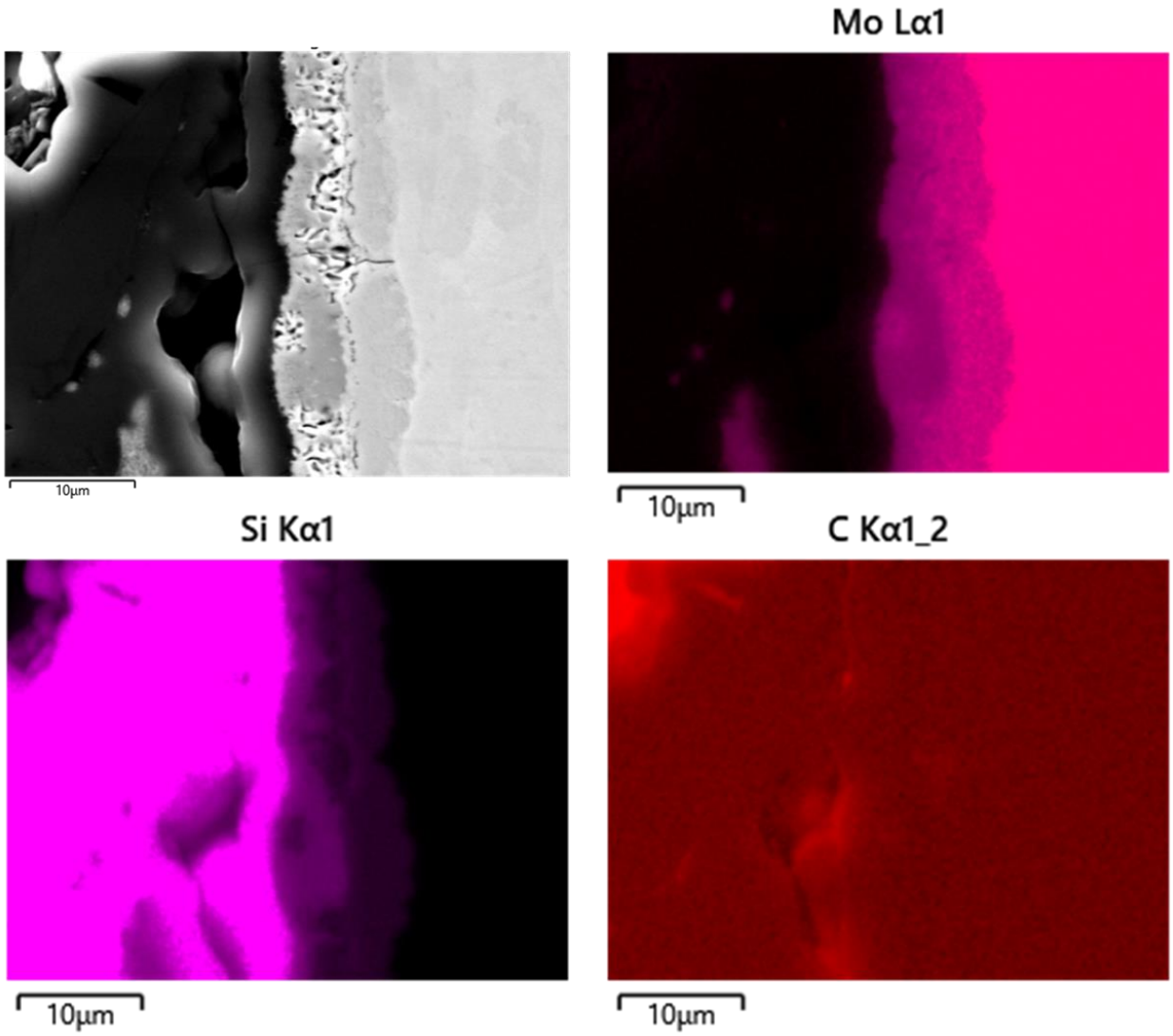

Figure 11. EDS maps showing elemental distributions near the Mo–SiC interface of an embedded Mo sheathed thermocouple.

Finally, indentations were performed to further characterize the interfacial bonding. Figure 12 shows microhardness measurements made using Vickers indentations on the Mo sheath. The microhardness values are consistent with those for bulk molybdenum metal (~2–2.5 GPa) [27]. Even at the highest applied load of 2,000 g (~20 N force), the measured microhardness does not decrease below what might be expected just due to increased slip and plastic deformation at higher loading. While this gives additional indications that the sheath is bonded to the SiC matrix, the applied shear stresses are still relatively low to calculate even a lower bound for the interfacial shear strength. For example, using the 20 N applied load and the nominal sheath diameter (1.6 mm) and bonded length (5.4 mm), the calculated shear stress is equal to 0.7 MPa.

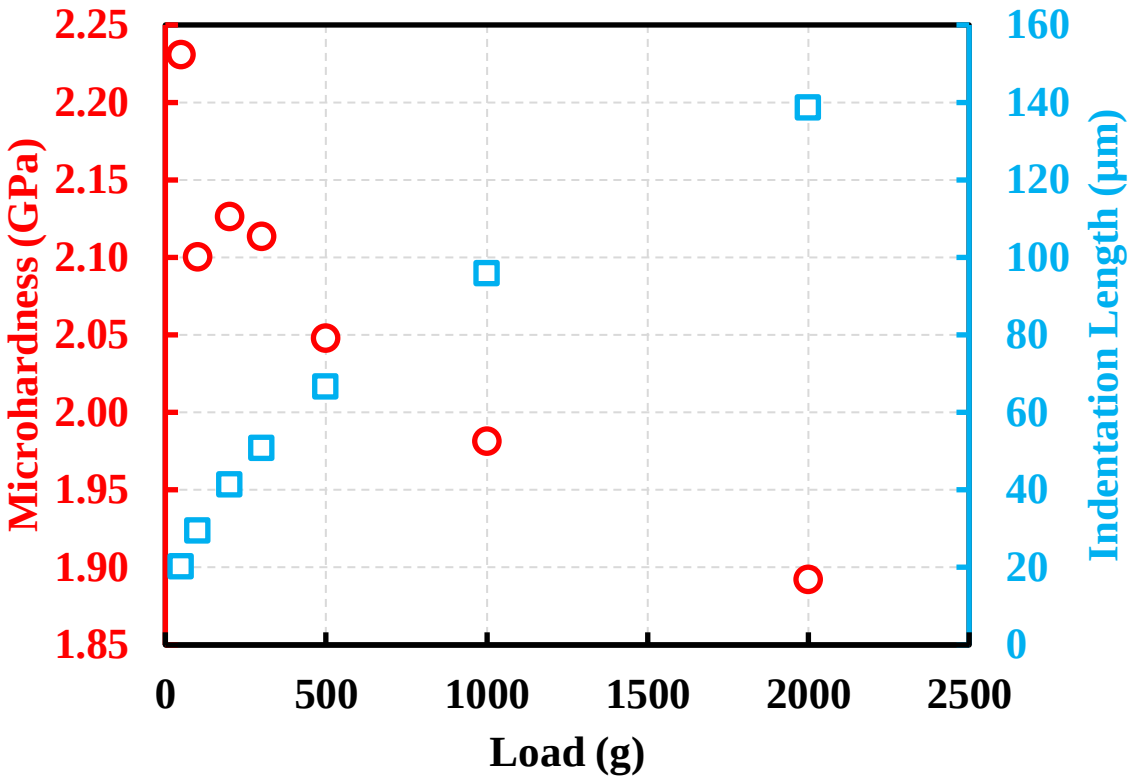

Figure 12. Vickers microhardness and indentation diagonal lengths vs. applied load on the Mo sheath of the embedded thermocouple.

Figure 13 shows nanohardness measurements that were performed across the Mo–SiC interface. Five indents were made on each side of the Mo-SiC interface using a load of 1 N using a 10-3-10 second trapezoidal load, hold, and unload program. As expected, the hardness is much higher in the SiC region compared to the Mo region. More importantly, the hardness does not decrease near the interface, providing additional evidence that the Mo sheath is bonded to the SiC matrix.

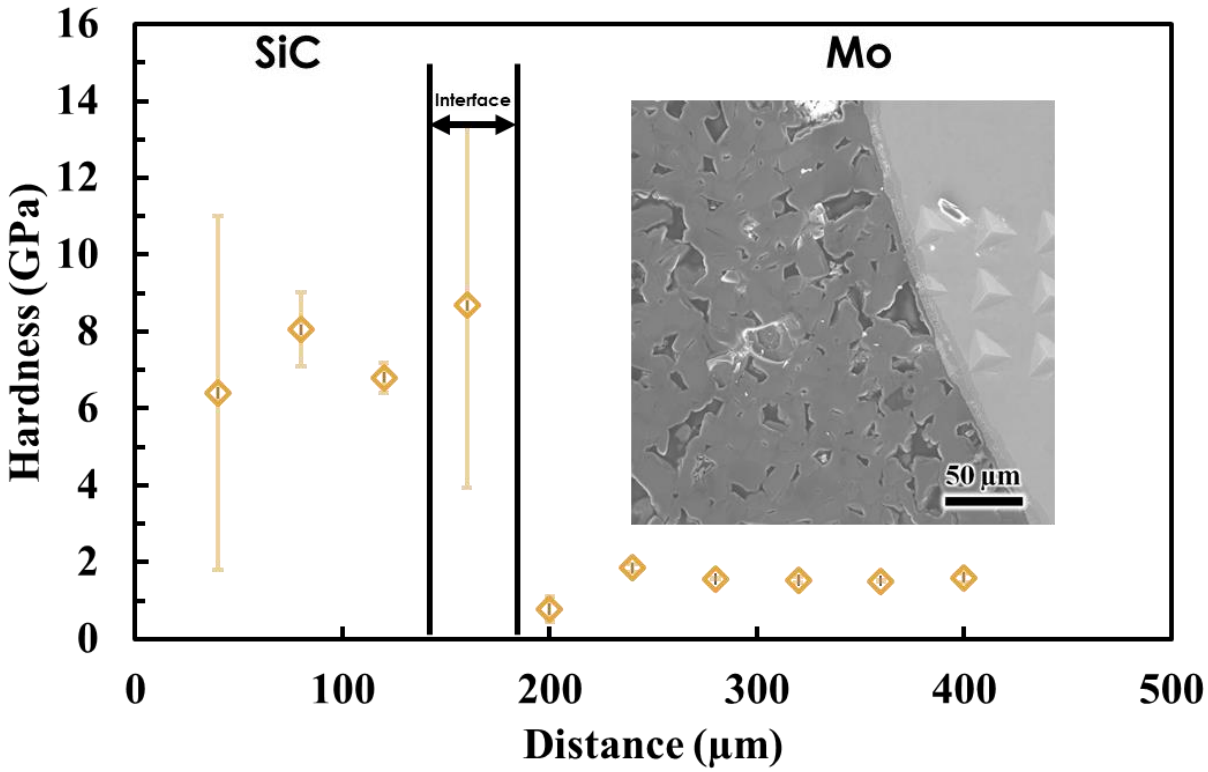

Figure 13. Local nanohardness measurements across the Mo–SiC interface, with indents shown in the inset view.

4. SUMMARY AND CONCLUSIONS

This report summarizes the advances that have been made in embedding functional sensors in 3D printed SiC components, including in situ measurements that were made during CVI. The sensor embedding procedure is described in more detail in a separate document that is available upon request. Mo-sheathed thermocouples were successfully embedded in SiC components during two separate CVI runs and were used to measure temperatures in situ during the embedding process. Distributed fiber-optic temperature sensors were able to resolve the temperature profile for part of the first day of one CVI run, but ultimately failed, likely due to issues with the fiber coating. Post-test characterization of the embedded thermocouples showed relatively uniform bonding between the sensors and the SiC matrix around the entire perimeter of the sensor. The fact that one embedded sensor remained bonded, even when the SiC component broke during disassembly, provides some indication of the strength of the bonding that occurs. EDS measurements at the interface revealed that the sensors do form a thin silicide layer, but the layer thickness (~10 μm) is only a small fraction of the overall sheath thickness (270 μm). Therefore, the sensor sheath is not expected to suffer from significant embrittlement during the embedding process. Future work will continue to investigate higher temperature coatings for the fiber-optic sensors and will move toward irradiation testing of embedded electrical sensors such as thermocouples and self-powered neutron detectors.

5. REFERENCES

1. B. Zohuri, *Nuclear micro reactors*. 2020, Cham, Switzerland: Springer.
2. C. M. Petrie et al., "Embedded metallized optical fibers for high temperature applications," *Smart Materials and Structures* 28 (2019) 055012.
3. C. M. Petrie et al., "High-temperature strain monitoring of stainless steel using fiber optics embedded in ultrasonically consolidated nickel layers," *Smart Materials and Structures* 28 (2019) 085041.
4. C. M. Petrie et al., "Embedded sensors in additively manufactured silicon carbide," *Journal of Nuclear Materials* 552 (2021) 153012.
5. C. M. Petrie and N. D. B. Ezell, *Demonstrate embedding of sensors in a relevant microreactor component*, ORNL/SPR-2020/1742, Oak Ridge National Laboratory, Oak Ridge, TN (2020).
6. D. C. Crawford et al., "An approach to fuel development and qualification," *Journal of Nuclear Materials* 371 (2007) 232–242.
7. D. C. Sweeney et al., "Metal-embedded fiber optic sensor packaging and signal demodulation scheme towards high-frequency dynamic measurements in harsh environments," *Sensors and Actuators A: Physical* 312 (2020) 112075.
8. B. Lu, H. Lan, and H. Liu, "Additive manufacturing frontier: 3D printing electronics," *Opto-Electronic Advances* 1 (2018) 170004.
9. M. T. Rahman et al., "Microscale additive manufacturing and modeling of interdigitated capacitive touch sensors," *Sensors and Actuators A: Physical* 248 (2016) 94-103.
10. ORNL. *Transformational Challenge Reactor: Demonstrating a faster, more affordable approach to advanced nuclear energy*. [cited 2020 1-26-2020]; Available from: tcr.ornl.gov.
11. B. R. Betzler et al., "Transformational Challenge Reactor preconceptual core design studies," *Nuclear Engineering and Design* 367 (2020) 110781.
12. K. A. Terrani et al., "Architecture and properties of TCR fuel form," *Journal of Nuclear Materials* (2021) 152781.
13. T. Ishikawa et al., "A Tough, Thermally Conductive Silicon Carbide Composite with High Strength up to 1600°C in Air," *Science* 282 (1998) 1295.
14. K. A. Terrani et al., "Silicon Carbide Oxidation in Steam up to 2 MPa," *Journal of the American Ceramic Society* 97 (2014) 2331–2352.
15. G. ERVIN JR., "Oxidation Behavior of Silicon Carbide," *Journal of the American Ceramic Society* 41 (1958) 347-352.
16. L. L. Snead et al., "Handbook of SiC properties for fuel performance modeling," *Journal of Nuclear Materials* 371 (2007) 329–377.
17. T. Koyanagi et al., "Mechanical property degradation of high crystalline SiC fiber–reinforced SiC matrix composite neutron irradiated to ∼100 displacements per atom," *Journal of the European Ceramic Society* 38 (2018) 1087–1094.
18. Y. Katoh et al., "Dimensional stability and anisotropy of SiC and SiC-based composites in transition swelling regime," *Journal of Nuclear Materials* 499 (2018) 471–479.
19. K. A. Terrani et al., "Irradiation stability and thermomechanical properties of 3D-printed SiC," *Journal of Nuclear Materials* 551 (2021) 152980.
20. N. M. George et al., "Neutronic analysis of candidate accident-tolerant cladding concepts in pressurized water reactors," *Annals of Nuclear Energy* 75 (2015) 703–712.
21. K. Terrani, B. Jolly, and M. Trammell, "3D printing of high-purity silicon carbide," *Journal of the American Ceramic Society* 103 (2020) 1575–1581.
22. C. M. Petrie et al., *Embedment of sensors in ceramic structures*, ORNL/SPR-2019/1301, Oak Ridge National Laboratory, Oak Ridge, TN (2019).
23. C. M. Petrie et al., *Demonstration of Embedded Sensors in Ceramic Structures*, ORNL/SPR-2020/1633, Oak Ridge National Laboratory, Oak Ridge, TN (2020).

24. M. Froggatt and J. Moore, "High-spatial-resolution distributed strain measurement in optical fiber with Rayleigh scatter," *Applied Optics* 37 (1998) 1735–1740.
25. T. W. Wood et al., "Evaluation of the Performance of Distributed Temperature Measurements with Single-Mode Fiber Using Rayleigh Backscatter up to 1000°C," *IEEE Sensors Journal* 14 (2014) 124–128.
26. D. C. Sweeney, A. M. Schrell, and C. M. Petrie, "An Adaptive Reference Scheme to Extend the Functional Range of Optical Backscatter Reflectometry in Extreme Environments," *IEEE Sensors Journal* 21 (2020) 498–509.
27. T. S. Srivatsan et al., "The microstructure and hardness of molybdenum powders consolidated by plasma pressure compaction," *Powder Technology* 114 (2001) 136-144.